Research Square

Preprints are preliminary reports that have not undergone peer review.
They should not be considered conclusive, used to inform clinical practice,
or referenced by the media as validated information.

A Study on Time-Varying Gain Inversion and Fault Detection Methods for Suspension Electromagnets in Maglev Trains under Under-determined Observation Conditions

Haining Liu
Taiyuan University of Science and Technology
Chenhua Liu
lchygs78@163.com
Taiyuan University of Science and Technology
Zhiqiang Han
Taiyuan University of Science and Technology

Research Article

Keywords: Maglev trains, electromagnetic force modeling, sparse symbolic regression, robust Bayesian inversion, time-series decomposition, fault diagnosis

Posted Date: November 23rd, 2026

DOI: https://doi.org/10.21203/rs.3.rs-11647133/v1

License: This work is licensed under a Creative Commons Attribution 4.0 International License.
Read Full License

Additional Declarations: No competing interests reported.

A Study on Time-Varying Gain Inversion and Fault Detection Methods for Suspension Electromagnets in Maglev Trains under Under-determined Observation Conditions

Abstract

Abnormal power-amplifier gains in maglev train suspension systems can compromise electromagnetic force regulation and complicate fault detection under noisy, underdetermined multi-channel conditions. To address these challenges, this paper proposes a fault identification method integrating physics-constrained modeling, robust Bayesian inversion, and structured time-series decomposition. First, electromagnetic monotonicity constraints are incorporated into sparse symbolic regression to improve the physical consistency of the force model. Second, electromagnetic forces are reconstructed using a two-degree-of-freedom train body–suspension frame model, and gain estimation is performed with a Student's t likelihood to reduce sensitivity to outliers. Third, Huber loss, low-rank–sparse decomposition, and temporal total variation regularization are combined to separate global gain drift from local channel faults. In a 16-channel, open-loop, parameter-driven simulation, the proposed method achieves an F1 score of 0.922 and a false positive rate of 1.46%. At an outlier ratio of 15%, the mean absolute gain-estimation error is 0.007. The mean detection delay across three controlled fault channels is 1.47 s, representing reductions of approximately 72.2% and 87.6% relative to standard robust principal component analysis and Kalman filtering, respectively. These results demonstrate the method's effectiveness under the tested simulation conditions.

Keywords: Maglev trains; electromagnetic force modeling; sparse symbolic regression; robust Bayesian inversion; time-series decomposition; fault diagnosis

1 Introduction

As a new type of rail transport system, maglev trains offer advantages such as contactless operation, low noise levels, high speeds and low energy consumption, and hold broad prospects for application in the fields of high-speed transport and urban rail transport. Lee et al. [1] provides an overview of maglev train technology, whilst Deng et al. [2] offers an outlook on the current state of maglev train development. The coupling between the electromagnetic attractive force generated by the suspension electromagnets and the vertical dynamic response of the train body–suspension frame system is the key factor determining operational stability [3]; the suspension gap, as a key variable characterising the system's operational state, directly influences the train's suspension stability and ride comfort [4].

During actual operation, abnormal gain in power amplifiers constitutes a fault mode that cannot be overlooked. Abnormal gain directly causes the electromagnetic force output to deviate from the design range, thereby leading to fluctuations in the suspension gap or even system instability [5]. In practical monitoring, only limited information—such as the suspension gap, vehicle body acceleration and current—can typically be obtained, whilst the parameters to be identified—the power amplification coefficients of each channel—exhibit time-varying behaviour, local abrupt changes and high-dimensional coupling characteristics, constituting a typical underdetermined observation problem [6]. The three core challenges in addressing this problem are as follows: firstly, there is a strong non-linear coupling between the electromagnetic force, current and gap; the required force model must therefore combine both data-fitting accuracy and physical plausibility; secondly, the

monitoring data inevitably contain sensor outliers and fat-tailed errors, and parameter estimation methods based on the traditional Gaussian noise assumption lack sufficient robustness under these conditions; thirdly, the time-varying evolution of multi-channel gains involves a mixture of two heterogeneous types of information: global common-mode drift and local fault disturbances; effectively separating the two under underdetermined conditions is a key prerequisite for accurate fault localisation.

In response to the aforementioned issues, scholars both in China and abroad have conducted relatively systematic research in areas such as electromagnetic force modelling, dynamic analysis and parameter inversion. With regard to electromagnetic force modelling, Ding et al. [7] employed a three-dimensional finite element method to perform numerical analysis on a high-speed maglev electromagnetic suspension system, investigating the influence of eddy current effects on the lifting force; however, such numerical methods involve significant computational overhead and make it difficult to derive explicit analytical expressions that can be directly used for real-time inversion; Mukhopadhyay et al. [8] established an electromagnetic force model and designed a control strategy for a magnetic levitation bearing system; however, as the modelling relies on specific structures and empirical parameters, its adaptability to different types of magnetic levitation systems is limited; Sun et al. [9] achieved good non-linear approximation results using neural networks, but the 'black-box' nature of the model limits its physical interpretability, posing certain obstacles to its direct application in safety-critical systems. The physically informed neural network proposed in Raissi et al. [10] embeds physical constraints into the neural network training process to balance fitting accuracy with physical consistency. The Sparse Symbolic Regression (SINDy) method proposed in Brunton et al. [11] is capable of automatically selecting dominant terms from a library of candidate functions and outputting explicit analytical expressions, thereby providing a new paradigm for mechanical modelling that balances accuracy and interpretability.

With regard to dynamic modelling, Li et al. [12] employed the Newtonian vector mechanics approach to establish the dynamic equations for a two-system suspension; whilst the physical picture is clear, the force analysis becomes rather cumbersome when extended to systems with multiple degrees of freedom; In contrast, the Lagrange–Rayleigh variational framework proposed in Goldstein et al. [13] provides a unified description of the system's kinetic energy, potential energy and dissipative characteristics from an energy perspective; whilst theoretically more suitable for modelling multi-degree-of-freedom coupled systems, its application in the field of maglev trains has not yet been fully documented. With regard to parameter inversion, traditional methods are mostly based on least-squares estimation [14] or Kalman filtering [15]; such deterministic methods are relatively sensitive to assumptions regarding the distribution of observation noise, and estimation accuracy declines significantly in the presence of fat-tailed noise or outliers. The Bayesian inference framework developed in Gelman et al. [16] is capable of integrating prior information and quantifying posterior uncertainty; however, its standard form typically models observation noise using a Gaussian distribution; Lange et al. [17] points out that the Student's t-distribution has heavier tails than the Gaussian distribution and, in theory, can provide a more robust noise model for statistical inference under conditions where outliers are present. With regard to fault detection, the Robust Principal Component Analysis (RPCA) proposed in Candès et al. [18] achieves structured separation of high-dimensional signals through low-rank–sparse decomposition, providing an effective mathematical tool for anomaly detection; however, it lacks time-series smoothing constraints.

In research into fault diagnosis for maglev suspension systems, the use of mathematical models and parameter-driven simulation to validate methods is not uncommon. Cui et al. [19] established a mathematical model of the suspension control system for maglev vehicles to address faults in the suspension signal, and explicitly used simulation to verify the effectiveness of the fault diagnosis method; Li et al. [20] established a non-linear model incorporating disturbances and network delays for the levitation control system of the CMS-04 maglev train, and conducted simulation-based fault diagnosis using actual system parameters; Wu et al. [21] recently employed MATLAB simulations to compare the Kalman observer, the unknown-input observer and a

dual-observer switching strategy for the fault diagnosis of active electromagnetic suspension systems. These studies demonstrate that, for potential faults that are difficult to introduce safely and reproducibly in a real-vehicle environment, numerical simulation based on reliable physical parameters can serve as a crucial means of method-level validation; however, its conclusions should be restricted to the scope covered by the model.

Furthermore, recent research on the non-linear vibrations of maglev vehicles, the dynamics of active magnetic levitation systems, and the influence of maglev model parameters has further expanded the scope of application of numerical modelling and simulation analysis. Among these, Kandil [22] presents an analytical and numerical study on the modelling and control of active magnetic levitation bearings; Ibrahim et al. [23] presents an analytical and RK4 numerical simulation of the vertical and lateral vibrations of maglev vehicles; Ibrahim et al. [24] investigates the displacement of the centre of vibration in maglev vehicles under aerodynamic forces; Kandil [25] analyses the non-linear dynamics and stability control of active magnetic levitation bearing systems; Kandil et al. [26] investigated the non-linear dynamics of a non-ideal magnetic levitation model; Francis et al. [27] examined the energy harvesting behaviour of a non-ideal magnetic levitation system. These studies provide a methodological basis for the model-driven simulation approach adopted in this paper to investigate the behaviour of levitation systems under complex operating conditions; however, this paper does not claim on this basis that full-scale vehicle validation has been completed.

With regard to method implementation and fault diagnosis evaluation, the Markov chain Monte Carlo method [28] provides a general numerical sampling framework for Bayesian posterior inference, whilst Huber robust statistics [29] and Lasso regularisation [30] provide theoretical tools for robust loss functions and sparse priors, respectively; Salfner et al. [31] provides a review of online fault prediction methods, whilst the IEEE Health Management Standard [32] and Isermann's monograph [33] present standardised evaluation frameworks for fault diagnosis. These methods provide the theoretical and tool-based foundation for the robust Bayesian inversion, structured sparse decomposition and fault evaluation discussed later in this paper.

Taking the current state of research into account, previous work has established a relatively robust methodological foundation in the three areas of electromagnetic force modelling, parameter estimation and fault detection; however, two structural shortcomings remain: Firstly, the selection of methods for each stage is relatively independent, lacking a systematic link from physical modelling to fault identification—the accuracy and physical consistency of the electromagnetic force model directly affect the reliability of subsequent parameter inversion, whilst the results of parameter inversion in turn constitute direct input for fault determination; there is an intrinsic, progressive interdependence between these three stages; Secondly, whilst the various methods place different emphases on aspects such as robustness, interpretability and adaptability to underdetermined systems, it is difficult to balance these requirements—the aforementioned methods each have shortcomings in terms of physical consistency, interpretability, noise assumptions and time-series smoothing, making it difficult to satisfy all requirements simultaneously.

Addressing the aforementioned shortcomings, this paper constructs a progressive analytical framework comprising physical constraint modelling, robust Bayesian inversion and structured sparse decomposition. Within this framework, the physical modelling of electromagnetic forces provides reliable force model inputs for subsequent stages; robust Bayesian inversion ensures statistical robustness for parameter estimation in the presence of noise; low-rank–TV structured decomposition enables precise fault localisation at the signal separation level, and a systematic comparison with existing methods is carried out under a unified evaluation metric system. Furthermore, to mitigate the risk of errors in upstream models propagating to downstream stages within the progressive chain, this paper incorporates model consistency checks, confidence thresholding and conservative fallback mechanisms into the outputs at each level: where the physical constraint model exceeds the training operating domain, the posterior uncertainty is excessive, or the ADMM residuals fail to converge, a

definitive fault conclusion is not directly output; instead, the status is marked as 'model uncertainty or requires review', thereby preventing a single link failure from causing the entire diagnostic chain to produce a false positive.

2. Models and Methods

In response to the three core bottlenecks outlined above, this chapter designs a progressive solution chain with tiered support, The first three sections sequentially carry out mechanism modelling, observation reconstruction and coarse screening of vehicle-wide faults, thereby enabling the final section to achieve single-channel fault decoupling and localisation. As errors in earlier stages propagate to subsequent stages, this paper further incorporates model operating domain checks, posterior uncertainty gating, ADMM convergence monitoring and a conservative fallback mechanism to prevent the failure of a single stage from directly invalidating the final diagnostic conclusion. Firstly, to address modelling inaccuracies, a compliant electromagnetic force model is constructed as the underlying input; this is then used to convert measured signals into electromagnetic observations. Subsequently, a Bayesian approach based on heavy-tailed noise is employed to perform an overall assessment of the vehicle's gain. Finally, a multi-constraint structured decomposition is utilised to distinguish between global, common drifts and local, sudden changes in individual channels. The complete solution process is as follows.

2.1 Explicit Modelling of Electromagnetic Forces

This section addresses the first bottleneck in modelling electromagnetic forces—the tendency to violate electromagnetic monotonicity—by incorporating inequality constraints into sparse symbolic regression, thereby deriving an analytical expression for electromagnetic forces that combines accuracy with physical interpretability, and providing a reliable excitation reference for subsequent dynamical solutions. The fundamental expression for electromagnetic forces is defined as follows:

$$F = \Phi\left(\tilde{I},\tilde{z}\right)c + \varepsilon \tag{1}$$

To eliminate redundant basis functions and ensure that the model is sparse and interpretable, an $L1$ regularisation term is introduced, and the optimisation objective function is formulated as follows:

$$\min_{c} \frac{1}{2}\|F - \Phi c\|_2^2 + \lambda\|c\|_1 \tag{2}$$

Embed monotonicity constraints from electromagnetism to ensure that the model outputs conform to objective electromagnetic laws:

$$\frac{\partial F}{\partial \tilde{I}} \geqslant 0, \frac{\partial F}{\partial \tilde{z}} \leqslant 0 \tag{3}$$

By discretising the partial derivative inequalities and converting them into linear constraints, a complete optimisation model with constraints is formed; solving this yields a sparse analytical formula for the electromagnetic force:

$$\begin{cases} \min\limits_{c} \frac{1}{2}\|F - \Phi c\|_2^2 + \lambda\|c\|_1 \\ s.t. Ac \leqslant b \end{cases} \tag{4}$$

Solve this constrained optimisation problem, automatically filtering out a small number of dominant

non-linear terms to obtain an electromagnetic force model that combines high accuracy, an explicit analytical form and physical monotonicity. This model serves as the external electromagnetic excitation for the vertical dynamics system comprising the vehicle body and suspension, and forms the underlying physical basis for the subsequent formulation of the dynamic observation equations and the inversion of the power amplifier gain parameters.

To address the issue of the applicability of physical constraints under boundary operating conditions, this paper restricts the monotonicity constraint to the operating domain $\Omega = [I_{\min}, I_{\max}] \times [z_{\min}, z_{\max}]$ covered by the modelling samples, without assuming that it can be extrapolated to arbitrary current and gap ranges. For operating conditions where the gap is below the rated value or where transient current surges occur, the constraint continues to participate directly in the model solution as long as the sample remains within Ω; if the operating point exceeds Ω, the operating domain boundary violation flag is triggered, and a conservative fallback to the boundary neighbourhood model or the basic physical model is employed, whilst preventing the independent triggering of a final fault conclusion during that time period. Consequently, both 'physical law constraints' and 'model applicability domain constraints' are incorporated into the safety protection logic.

2.2 Modelling of vertical dynamics

Based on the analytical expression for the electromagnetic force derived in Section 2.1, a mechatronic coupling dynamic system is established. By utilising the measurable suspension gap and acceleration, the electromagnetic observation force—which cannot be measured directly—is inverted, thereby providing effective observational data for the subsequent inversion of gain parameters. To establish a link between the measured signals and the electromagnetic forces, whilst balancing computational efficiency and modelling accuracy, the vertical displacement of the vehicle body z_b and the vertical displacement of the suspension frame z_f are selected as generalised coordinates, denoted as $q = [z_b, z_f]^T$, thereby establishing a two-degree-of-freedom dynamic model for the vehicle body–suspension frame system:

The known formulae of classical mechanics are:

$$T = \frac{1}{2} m_b \dot{z}_b^2 + \frac{1}{2} m_f \dot{z}_f^2 \tag{5}$$

The potential energy of the system comprises gravitational potential energy and the elastic potential energy of the air spring:

$$V = \frac{1}{2} k_s (z_b - z_f)^2 + m_b g z_b + m_f g z_f \tag{6}$$

The Rayleigh dissipation function describes energy loss due to damping:

$$D = \frac{1}{2} c_s (\dot{z}_b - \dot{z}_f)^2 \tag{7}$$

Substituting into the standard general equations of Lagrange–Rayleigh dynamics:

$$\frac{d}{dt}\left(\frac{\partial T}{\partial \dot{q}_i}\right) - \frac{\partial T}{\partial q_i} + \frac{\partial V}{\partial q_i} + \frac{\partial D}{\partial \dot{q}_i} = Q_i \tag{8}$$

Finally, by substituting the kinetic energy, potential energy and dissipation function into the equation, and separating the two degrees of freedom of the vehicle body and the suspension, we obtain the complete system of differential equations for the two-degree-of-freedom vertical dynamics:

$$m_b \ddot{z}_b + k_s (z_b - z_f) + c_s (\dot{z}_b - \dot{z}_f) + m_b g = 0 \tag{9a}$$

$$m_f \ddot{z}_f - k_s(z_b - z_f) - c_s(\dot{z}_f - \dot{z}_b) + m_f g = F\left(\tilde{I}, \tilde{z}\right) \quad (9b)$$

The body-suspension dynamic model characterises the elastic-damped coupling relationship between the vehicle body and the suspension, and introduces electromagnetic forces to achieve electromechanical coupling; furthermore, by substituting gap and acceleration data, the observed electromagnetic forces can be inverted, thereby providing observation equations for Bayesian inversion. With regard to numerical solution, the RK45 adaptive step size algorithm is employed to perform time-domain integration of the system of differential equations; this method offers high computational efficiency whilst ensuring accuracy.

It should be noted that this paper employs a two-degree-of-freedom (2-DOF) model to establish a low-order inversion mapping between observable signals and electromagnetic forces; it does not constitute a complete reproduction of the various coupling effects present in a full-scale maglev train system. In actual 16-channel maglev systems, complex higher-order dynamic effects such as current crosstalk, magnetic field cross-coupling, and vehicle pitch and roll exist; this paper collectively classifies such unmodelled dynamics as observation disturbances and model uncertainties. On this basis, by introducing the Student's t-likelihood and the Huber loss function, the interference resistance and robustness of the subsequent state estimation process are effectively enhanced. In terms of model generalisability, the Lagrange–Rayleigh modelling framework adopted in this paper can be directly extended to systems with a high number of degrees of freedom; however, an increase in degrees of freedom significantly increases the dimensionality of the state equations and the computational overhead of inversion. Therefore, in practical applications, techniques such as model reduction, sliding-window iteration or parallel solving must be combined to ensure the system's ability to respond rapidly to faults.

2.3 Development of a Robust Bayesian Inversion Framework

Based on the theoretical electromagnetic forces and the inverted observational forces described in the preceding section, the Student's t-distribution with heavy tails is introduced to improve the Bayesian estimation. To resolve the logical discontinuity between the 'uniform vehicle-wide gain of η' and the subsequent 'multi-channel gain matrix', this paper defines the vehicle-wide gain of η_g as the common-mode reference for the multi-channel gains, whilst simultaneously constructing a rough estimate of the time-varying gain $\eta_i(t)$ for each electromagnet channel. η_g is used for the preliminary assessment of global drift at the vehicle-level, whilst $\eta_i(t)$ serves as the direct input to the joint decomposition model in Section 2.4; consequently, Section 2.3 does not merely output a single scalar, but rather produces two tiers of results: a global reference and channel-specific time-series gains. The vehicle-wide unified gain is used solely for the initial screening of drift at the vehicle level, whilst the input fed into the joint identification model in Section 2.4 is the multi-channel time-series gain matrix.

First, let the i-th channel's observed electromagnetic force, derived from the dynamical model, be $F_i^{obs}(t)$, and the theoretical force calculated from the explicit electromagnetic force model be $F_i^{th}(t)$. After taking into account the gain of the power amplifier, a rough gain estimation model is established using the channel-specific observation relationships. For any given instant, the ratio of the observed force to the theoretical force in each channel can be used to form a candidate value for the channel gain, which is then subjected to a robust posterior estimation under the Student's t-likelihood.

$$\eta_i(t) = F_i^{obs}(t) / F_i^{th}(t), i = 1, 2, ..., M; \quad (10)$$

$$\eta_g(t) = RobustAggregate\{\eta_1(t), ..., \eta_M(t)\} \quad (11)$$

Of these, $\eta_i(t)$ retains channel-level timing information, whilst $\eta_g(t)$ merely characterises global common-mode variations. To avoid ratio amplification noise when the theoretical force approaches zero, this

ratio is calculated only within the valid observation interval of $|F_i^{th}(t)| \geqslant \varepsilon_F$; the remaining points are estimated continuously using a posteriori models.

$$F_{obs}(t) = \eta F_{model}(t) + \varepsilon(t) \tag{12}$$

In this context, in Equation (10), represents the unified vehicle-level gain obtained by aggregating the rough estimates of the time-varying gains from each channel; consistent with the meaning described above, it is used to characterise variations in common-mode gain at the vehicle level; denotes the observed electromagnetic force obtained by inverting the body–suspension dynamic model based on measurable signals such as suspension clearance and acceleration; denotes the theoretical electromagnetic force calculated using the physically constrained electromagnetic force model described in Section 2.1; denotes the stochastic residual between the observed electromagnetic force and the gain-corrected theoretical force, which is primarily used to describe sensor noise, model errors and unmodelled disturbances. Consequently, Equation (10) links the observed electromagnetic force, the theoretical electromagnetic force, the unified gain and the random residual at the vehicle level, forming a statistical observation relationship, whilst the channel level retains the channel time-series information required for the joint decomposition described in Section 2.4.

By abandoning the traditional Gaussian noise assumption and instead using a Student's t-distribution with a heavier tail to describe the residual noise, the model automatically and adaptively applies reduced weights to outliers with large residuals, thereby minimising the interference of anomalous data on parameter estimation:

$$\varepsilon(t) \sim t_v(0, \sigma^2) \tag{13}$$

Set the prior distribution for the gain $N(1.0, 0.2^2)$, and derive the posterior distribution using Bayes' theorem in conjunction with the likelihood function:

$$p(\eta|D) \propto p(D|\eta)\, p(\eta) = \Pi_{t=1}^{T} t_v(F_{obs}(t)\,|\eta F_{model}(t), \sigma^2) \cdot N(\eta|1.0, 0.2^2) \tag{14}$$

Finally, the Markov Chain Monte Carlo (MCMC) method [28] was employed for numerical sampling, and the parameters were quantitatively evaluated using the posterior mean, maximum a posteriori (MAP) estimates and the 95 per cent highest posterior density (HPD) confidence interval. If the posterior credibility interval for a parameter consistently deviates from the normal range, a gain drift at the vehicle-level is deemed to exist; if local deviations occur only in a few channels, a vehicle-level fault is not directly diagnosed, but the issue is referred to the low-rank–sparse–TV joint decomposition described in Section 2.4 for further localisation. Furthermore, when the posterior credibility interval is excessively wide, the MCMC fails to meet the convergence criteria, or the number of valid samples is insufficient, the system outputs an 'estimate uncertain' flag rather than a definitive fault conclusion.

2.4 Development of a Joint Recognition Model

The output $\eta_g(t)$ from Section 2.3 is used to characterise the global common-mode trend, whilst the $M \times T$ -dimensional multi-channel time-domain gain matrix $Y = [\eta_i(t)]$ serves as the direct input to this section. Consequently, the low-rank component L primarily captures the slowly varying background formed by η_g and the common response between its channels, whilst the sparse component S describes local anomalies in a small number of channels. This structure clarifies the data transfer relationship between the coarse estimation of the vehicle-wide gain and the decoupling of single-channel faults; it also enables the posterior uncertainty from Section 2.3 to be further suppressed in Section 2.4 via the Huber data fidelity term.

First, let us assume that the system comprises *N* electromagnets and that the observation window contains *T*

sampling times. The estimated gain values at each time step are organised into an observation matrix as follows:

$$E_{obs} = [\eta_i(t_j)] \in R^{N \times T} \ , i = 1, 2, ..., N \ \ j = 1, 2, ..., T \tag{15}$$

In this context, each row of the matrix corresponds to the time series of each channel, whilst each column corresponds to a snapshot of the channel gain at a given instant. Furthermore, the Huber loss [29] is employed to construct a data fidelity term, with the aim of enhancing the model's robustness to outliers; simultaneously, the kernel norm is used to constrain low-rank components, the norm is used to constrain sparse components, and a total temporal variance regularisation term is introduced to suppress transient fluctuations whilst preserving the temporal structure of faults:

$$E = L + S \tag{16}$$

To balance the four requirements of outlier robustness, global drift separation, local fault extraction and time-series smoothing constraints, four types of constraints are introduced to formulate a joint optimisation objective:

$$\min_{L,S} J(L,S) = \sum_{i=1}^{N} \sum_{j=1}^{T} \ell_\delta \left((E_{obs})_{ij} - L_{ij} - S_{ij} \right) + \lambda_1 \|L\|_* + \lambda_2 \|S\|_1 + \lambda_3 \|L + S\|_{TV} \tag{17}$$

In particular, this model employs the Huber loss as a data fidelity term to reduce the weight of extreme outliers in the residuals, whilst introducing a kernel norm $\|L\|_*$ to impose constraints on low-rank components. This serves to extract common, slow drifts present across all channels, and is combined with an L_1 norm $\|S\|_1$ to constrain sparse components, thereby highlighting local fault-induced sudden changes originating from a small number of channels. further supplemented by time-domain TV total variation regularisation $\|L+S\|_{TV}$ to constrain the smooth evolution of gain over time, which not only filters out meaningless transient random fluctuations but also fully preserves the step-change boundaries corresponding to faults.

In Equation (15), the first term serves to enhance robustness against residual noise and outliers; the second term characterises global common-mode variations in multi-channel gain; the third term is used to extract local anomalies in a small number of channels [30]; and the fourth term constrains the smooth evolution of gain over time. The combined effect of these four terms can effectively improve the model's identifiability under underdetermined conditions.

It should be noted that, in the current joint decomposition model, the fault semantics are still limited to 'abnormal power amplifier gain'. Sensor bias, sensor drift, changes in vehicle mass and structural wear may all generate abnormal residuals in the observation matrix; however, the existing underdetermined observations alone do not guarantee that these can be uniquely distinguished from power amplifier gain faults. Consequently, this paper does not claim that the model is capable of directly achieving full isolation of multiple faults; should the analysis need to be extended to sensor faults or changes in vehicle mass, corresponding latent variables or a structured dictionary should be incorporated into the model, and joint identification should be performed by utilising the differences in current, air gap, acceleration and frequency-domain responses between various faults.

2.5 Model solving

With regard to the joint recognition model constructed in Section 2.4, as the objective function simultaneously includes the Huber robust loss, a kernel norm constraint, a sparsity constraint and a total temporal variance regularisation term, the overall optimisation problem is characterised by non-smoothness and strong coupling, making it difficult to obtain a stable solution using direct gradient methods.

To this end, this paper employs the Alternating Direction Method of Multipliers (ADMM) to perform variable splitting on the original problem, thereby transforming the complex optimisation problem into a number of

decomposable sub-problems. Through block-by-block iteration, it achieves a joint estimation of low-rank background, local faults and temporal disturbances. The solution process is as follows:

To meet the conservative diagnostic requirements of safety-critical systems, three types of failure protection have been implemented in the ADMM solution process:

(1) If the original residuals and dual residuals do not reach the threshold within the maximum number of iterations, a 'non-convergence' status is output; no fault channel localisation results are provided, and the status is marked as 'Solution did not converge; review required';

(2) A review of the results is triggered when the energy proportions of low-rank and sparse components exceed the permissible range specified for the validation set;

(3) Relying solely on this module to provide a final fault conclusion is prohibited when the model operating domain is exceeded or when the prior-posterior uncertainty in the preceding stage is excessive.

Firstly, let the observation gain matrix be $X\epsilon\mathbb{R}^{N\times T}$, and convert the time-domain TV regularisation equivalently into the form of a first-order difference operator in the time dimension, yielding a unified unconstrained optimisation objective:

$$\min_{L,S}\sum_{i,j}\rho_{\delta}\left(X_{ij}-L_{ij}-S_{ij}\right)+\lambda_1\|L\|_*+\lambda_2\|S\|_1+\lambda_3\|D(S)\|_1 \tag{18}$$

Here, L denotes the low-rank common-mode drift component, S denotes the sparse fault component, μ is the *ADMM* penalty coefficient, δ is the Huber loss threshold, $\rho_{\delta}(\cdot)$ is the Huber loss function, $D(\cdot)$ denotes the first-order difference operator along the time dimension, and $\|D(S)\|_1$ is the *TV* regularisation term.

The Huber loss function in piecewise form is then introduced; on the one hand, it maintains a quadratic smoothing fit for small residuals, whilst on the other hand, it linearly weights out large outlier residuals, thereby mitigating the estimation interference caused by sensor anomalies:

$$\rho_{\delta}(e)=\begin{cases}\dfrac{1}{2}e^2, & |e|\leqslant\delta\\[2ex] \delta|e|-\dfrac{1}{2}\delta^2, & |e|>\delta\end{cases} \tag{19}$$

As the variables L and S in the original optimisation formula are highly coupled and the various regularisation terms cannot be separated individually, auxiliary variables E, V and Z are introduced to represent the residual term, the sparse components and the time-domain difference results, respectively. In conjunction with three sets of equality constraints, this transforms the unconstrained minimisation problem into an equivalent constrained optimisation problem; that is, complete decoupling of the different regularisation terms is achieved through variable decomposition:

$$\min_{L,S,E,V,Z}\sum_{i,j}\rho_{\delta}\left(E_{ij}\right)+\lambda_1\|L\|_*+\lambda_2\|V\|_1+\lambda_3\|Z\|_1 \tag{20}$$

The constraints are as follows:

$$\begin{gathered}s..t.X=L+S+E\\ S=V\\ Z=D(S)\end{gathered} \tag{21}$$

Secondly, in order to solve this convex optimisation problem subject to the given set of equality constraints, we further construct an augmented Lagrangian function incorporating scaled Lagrangian multipliers and a penalty term:

$$L_\mu = \sum_{i,\ j} \rho_\delta\left(E_{ij}\right) + \lambda_1 \|L\|_* + \lambda_2 \|V\|_1 + \lambda_3 \|Z\|_1 + \frac{\mu}{2}\|X - L - S - E + U_1\|_F^2 + \frac{\mu}{2}\|S - V + U_2\|_F^2 + \frac{\mu}{2}\|D(S) - Z + U_3\|_F^2 \quad (22)$$

Subsequently, based on the core concept of *ADMM*'s alternating iterations, the Lagrangian function is minimised for a single variable whilst holding all other variables constant, and this process is repeated to update each variable in turn. When updating the low-rank component L, the remaining variables are treated as constants, leaving only the kernel norm and the augmented quadratic penalty term to form a quasi-terminal problem. To rapidly obtain an exact optimal solution, a singular value threshold operator is employed to perform low-rank contraction on the matrix, thereby deriving the following update equation:

$$L^{k+1} = \mathrm{SVT}_{\lambda/\mu}(X - S^k - E^k + U_1^k) \quad (23)$$

and the *SVT* operator calculation formula, which is used to isolate the global gain drift component of the full-channel common-mode:

$$\mathrm{SVT}_\tau(A) = U\,\mathrm{diag}\left((\sigma_i - \tau)_+\right)V^T \quad (24)$$

Among these, the truncation operator satisfies $(x)_+ = \max(x, 0)$, whilst σ_i is a singular value.

Subsequently, update the residual variable *E* and construct an intermediate matrix to isolate the quadratic term corresponding to the Huber loss as follows:

$$V_E^k = X - L^{k+1} - S^k + U_1^k \quad (25)$$

Furthermore, by distinguishing between normal residuals and outliers based on the principle of proximal mapping, we derive the piecewise closed-form update equation:

$$E^{k+1} = \mathrm{prox}_{\delta/\mu}(V_E^k) \quad (26)$$

$$E_{ij}^{k+1} = \begin{cases} \dfrac{\mu}{\mu+1} v_{ij}, & |v_{ij}| \leqslant \left(1 + \dfrac{1}{\mu}\right)\delta \\ v_{ij} - \dfrac{\delta}{\mu}\mathrm{sgn}(v_{ij}), & |v_{ij}| > \left(1 + \dfrac{1}{\mu}\right)\delta \end{cases} \quad (27)$$

Of these, v_{ij} are elements of V_E^k; this update automatically reduces the weights under conditions of large residuals, thereby suppressing the influence of outliers.

Furthermore, to eliminate the need for a sub-gradient, we directly take the derivative of the objective function and set it to zero, which, upon simplification, yields a banded sparse system of linear equations:

$$S^{k+1} = \arg\min_S \frac{\mu}{2}\|X - L^{k+1} + S - E^{k+1} + U_2^k\|_F^2 + \frac{\mu}{2}\|S - V^k + U_2^k\|_F^2 + \frac{\mu}{2}\|D(S) - Z^k + U_3^k\|_F^2 \quad (28)$$

This problem corresponds to a quadratic optimisation problem with a differential term, which can be reformulated as a system of linear equations to be solved:

$$(2I + D^T D)S^{k+1} = X - L^{k+1} - E^{k+1} + U_1^k + V^k - U_2^k + D^T(Z^k - U_3^k) \quad (29)$$

Of these, D^T are the adjoint operators of *D*. As $D^T D$ exhibits a sparse banded structure in the time dimension, this linear system can be solved efficiently using the conjugate gradient method or sparse Cholesky decomposition.

In terms of computational complexity, the primary computational overhead for the current settings of *M=16* and *T=40,000* stems from the singular value decomposition (SVD) of low-rank updates and the solution of time-domain banded linear systems. For a fixed channel size of 16, the matrix updates in a single *ADMM*

iteration increase primarily with the length of time *T*; in engineering applications, sliding time windows, truncation, or random *SVD* and warm-start strategies may be employed to reduce the computational burden of a single update.

It should be noted that the primary objective of the *ADMM* solution process described in this paper is to ensure the stable convergence of the joint decomposition model and the effective separation of low-rank, sparse and time-varying components, rather than to optimise real-time computation for specific in-vehicle hardware. The algorithm monitors the convergence of the iterative process via the original and dual residuals, terminating the iteration when a preset threshold is reached; if the convergence conditions are not met within the maximum number of iterations, the algorithm outputs a 'non-converged' status and triggers a review of the results. For practical deployment, the computational burden of the algorithm is primarily related to the observation window length, the number of channels, the scale of the singular value decomposition, and the number of *ADMM* iterations; the scale of the upstream *MCMC* sampling also affects the overall diagnostic cycle. Therefore, this paper analyses the feasibility of the solution process solely from the perspective of algorithmic structure and makes no quantitative commitments regarding end-to-end real-time computational performance on specific in-vehicle platforms; relevant performance still requires further testing on a unified hardware platform or in a hardware-in-the-loop environment.

To induce channel sparsity and filter out temporal random fluctuations, a soft-thresholding operator is used to contract the values element-by-element, updating the auxiliary variables *V* and *Z* respectively:

$$V^{k+1} = \mathrm{Soft}_{\lambda_S/\mu}\left(S^{k+1} + U_2^k\right) \tag{30}$$

The soft thresholding operator is defined as follows:

$$\mathrm{Soft}_{\tau}(x) = \mathrm{sgn}(x)\max(|x| - \tau, 0) \tag{31}$$

$$Z^{k+1} = \mathrm{Soft}_{\lambda_S/\mu}\left(D(S^{k+1}) + U_3^k\right) \tag{32}$$

After completing a round of iterations using the original variables, in order to correct constraint deviations and ensure the convergence accuracy of subsequent iterations, the Lagrangian dual multipliers are updated based on the residuals from the three sets of equality constraints:

$$U_1^{k+1} = U_1^k + X - L^{k+1} - S^{k+1} - E^{k+1} \tag{33}$$

$$U_2^{k+1} = U_2^k + S^{k+1} - V^{k+1} \tag{34}$$

$$U_3^{k+1} = U_3^k + D(S^{k+1}) - Z^{k+1} \tag{35}$$

The algorithm terminates when one of the following convergence conditions is satisfied:

$$\frac{\|X - L^k - S^k - E^k\|_F}{\|X\|_F} < \varepsilon,\ \frac{\|S^k - V^k\|_F}{\|S^k\|_F} < \varepsilon,\ \frac{\|D(S^k) - Z^k\|_F}{\|D(S^k)\|_F} < \varepsilon$$

In this context, the convergence threshold is set to $\varepsilon \epsilon [10^{-5},\ 10^{-4}]$ by default in the programme.

The complete variable iteration process requires iterative execution until the relative *F*-norms of the residuals for all three sets of constraints are all below the preset minimum threshold of ε, at which point the algorithm is deemed to have converged. Once convergence is achieved, in order to distinguish the severity of faults across different channels, the L2-norm fault index e_i is calculated row by row using the sparse fault component *S*, according to the following formula:

$$e_i = \| S_{i,:} \|_2 \tag{36}$$

Finally, by combining this with the time indices corresponding to the non-zero elements of S, it is possible to simultaneously identify the faulty solenoid channel and the time period during which the anomaly occurred, thereby achieving the decoupled identification of global gain drift and local channel faults under underdetermined observation conditions.

3. Numerical simulation validation and analysis of engineering applicability

3.1 Simulation Settings

The simulation dataset used in this paper was constructed based on publicly available technical parameters of the suspension system for a specific type of medium- to low-speed maglev train, as well as relevant literature; the main physical parameters are shown in Table 1. The dataset comprises 16 electromagnet channels, with a sampling frequency of 200 Hz and a single observation duration of 200 s; consequently, a total of 40,000 sample points are obtained for each channel, forming a *16×40,000* multi-channel time series. To enhance the engineering realism of the data, Gaussian noise with a mean of zero and a standard deviation of 2.5 per cent of the signal amplitude was superimposed onto the observations in each channel. Furthermore, outliers were randomly injected at a rate of 5 per cent to 15 per cent, with amplitudes approximately 10 to 15 times the standard deviation of the normal noise, to simulate sporadic sensor anomalies. Faulty samples were generated by attenuating the power amplification factor of specified channels by 25 per cent to 40 per cent; a total of three controlled fault channels were set up (Ch. 1, Ch. 3 and Ch. 10).

Furthermore, to test the method's ability to suppress transient anomalies, drift interference lasting approximately 9 seconds and with an amplitude of approximately 0.24 was injected into normal channels Ch.5 (70–79 s) and Ch.13 (148–157 s), respectively. The dataset was split into training, validation and test sets in a ratio of 60%:20%:20%. Model parameters were fitted using the training set, hyperparameters were selected using the validation set, and final performance was evaluated on the test set. All comparison methods employed the same data partitioning, fault settings and evaluation criteria. To prevent long periods of normal data from diluting the fault detection metrics, this paper calculated *TP*, *FP*, *TN* and *FN* solely within the fault-related windows of the test set, comprising a total of 6,400 samples.

This paper employs a parameter-driven numerical simulation, constructed using publicly available technical parameters and relevant literature, to validate the methodology. Given that gain anomalies in power amplifiers involve the closed-loop state of the suspension control system, artificially introducing faults into operational vehicles would alter the system's normal operating state and introduce unacceptable safety risks; furthermore, it is difficult to obtain multi-channel synchronised data from actual lines that includes complete fault truth values, controllable disturbance intensities and clearly defined fault durations. Consequently, this paper limits the scope of verification to a feasibility analysis at the model and algorithm levels, focusing on examining the effectiveness of the proposed method in terms of physical constraints, fault distinguishability, and resistance to noise and anomalies, without equating the simulation results directly with the actual operational performance of vehicles.

It should be noted that this paper employs open-loop dynamic simulation and does not explicitly incorporate a closed-loop suspension controller or its compensation mechanism for variations in power amplifier gain; consequently, the present results primarily reflect the performance of the algorithm under the established open-loop dynamic model and the specified disturbance conditions; This paper has not yet conducted tests on the minimum detectable gain attenuation under closed-loop control conditions; consequently, it is not possible to

determine the fault detection threshold or detection boundary for an actual closed-loop system on this basis. The compensatory behaviour of the closed-loop controller and its impact on fault distinguishability require further investigation in subsequent research.

To improve the correspondence between verification scenarios and monitoring conditions, controlled disturbances—such as observational noise, outliers, global drift and local gain anomalies—were introduced into the simulation data, and repeatable comparisons were conducted using standardised data segmentation and evaluation metrics. This validation approach is consistent with the methods employed in existing research on magnetic levitation suspension fault diagnosis, which utilise mathematical models and actual system parameters for numerical simulation; the works cited in References [19], [20] and [21] all adopt this approach. It should be noted that the aforementioned disturbances and faults are all model-based constructs; their primary purpose is to establish a validation environment with clearly defined true values and controllable intensities. Consequently, the results obtained are used to evaluate the relative performance of the algorithm within a given model and disturbance range, rather than to replace actual measurement data from the circuit.

Table 1 Main Physical Parameters of the Simulation System

Parameter	Symbol	Value	Unit
Equivalent mass of vehicle body	m_b	2500	kg
Equivalent mass of levitation bogie	m_f	800	kg
Equivalent stiffness of air spring	k_s	1.2×105	N/m
Damping coefficient of secondary suspension	c_s	5.0×103	N·s/m
Rated levitation gap	z_{nom}	0.09	m
Rated current	I_{nom}	20	A
Number of electromagnet channels	N	16	—
Sampling frequency	f_s	200	Hz
Single observation duration	T_{obs}	200	s
Sampling points per channel	$M = f_s T_{obs}$	40000	points

3.2 Fault Detection Performance Indicator 1: Comparison of Fault Detection Accuracy

Fault detection can essentially be reduced to a binary classification problem at each sampling point. Let $\mathcal{F}_{true}$ denote the set of monitored fault samples, and $\mathcal{F}_{pred}$ the set of samples classified as faults by the method. Based on this, true positives (TP), false positives (FP), true negatives (TN) and false negatives (FN) can be calculated, and metrics such as precision, recall, F_1 score and false positive rate (FPR) can be further computed [31][32]. Existing research [31][32] indicates that these four metrics provide a relatively comprehensive reflection of the performance of fault detection algorithms in practical applications; therefore, this paper adopts them as the basis for evaluating detection accuracy:

$$Precision = \frac{TP}{TP + FP}$$

$$\mathrm{Re}call = \frac{TP}{TP + FN}$$

$$F_1 = \frac{2 \times Precision \times \mathrm{Re}call}{Precision + \mathrm{Re}call}$$

$$F_1 = \frac{2 \times Precision \times \mathrm{Re}call}{Precision + \mathrm{Re}call}$$

$$FPR = \frac{FP}{FP + TN}$$

To provide a visual illustration of the discriminative performance of the six methods in the task of fault detection at individual sampling points, this paper further presents the fault detection results in the form of a binary classification confusion matrix and visualises a comparison of the predictions for normal and faulty samples. Specifically, Figure 1 illustrates the differences between the methods in terms of four statistical metrics: true positives (*TP*), false positives (*FP*), true negatives (*TN*) and false negatives (*FN*), thereby providing a clearer picture of the performance of different methods across the two dimensions of 'fault detection' and 'false alarm suppression'. Since fault detection in practical engineering not only requires capturing as many anomalous samples as possible but also necessitates avoiding the misclassification of normal fluctuations as faults, it is difficult to comprehensively evaluate the merits of different methods based on a single metric alone. Accordingly, Figure 1 provides a comprehensive comparative analysis of the fault detection capabilities of the six methods at each data point, incorporating metrics such as *Precision*, *Recall*, *F1* score and *FPR*.

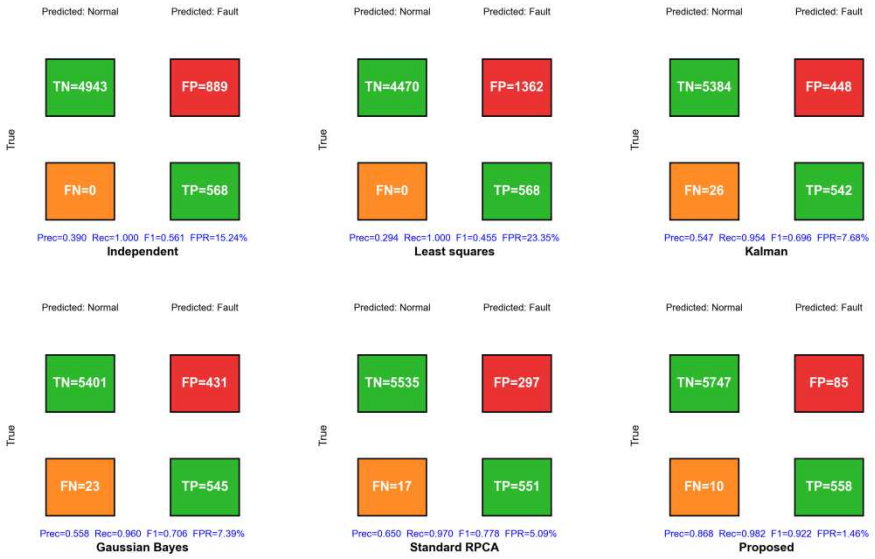

Figure. 1 Accuracy metrics: quantitative detection results for each sampling point (a) independent method (b) least squares method [14] (c) Kalman+CUSUM [15] (d) Gaussian Bayesian [16] (e) standard RPCA [18] (f) the method proposed in this paper (low-rank + TV)

As can be seen from the comparison of fault detection metrics for the six methods in Figure 1, there are significant differences in the trade-offs between fault recall and false alarm rate across the various methods. Firstly, whilst the Independent and Least Squares methods do not miss any faults and achieve a perfect recall score, they exhibit extremely high numbers of false alarms and false alarm rates, as well as a relatively low precision rate, making them prone to misclassifying normal fluctuations as faults; Secondly, whilst Kalman+CUSUM and the Gaussian Bayesian approach, which rely on statistical models, slightly reduce false

alarms, they still exhibit a considerable number of false alarms and a small number of missed faults; furthermore, although standard *RPCA* further optimises performance metrics through low-rank decomposition, it cannot completely eliminate false alarms due to the lack of temporal constraints. In contrast, the LowRank+*TV* method proposed in this paper, which integrates low-rank decomposition, *TV* regularisation and Huber robust loss, not only significantly reduces the false positive rate to 1.46 per cent whilst maintaining a high recall rate of 0.982, but also achieves a precision of 0.868 and an *F1* score of 0.922—both of which are the best among the six methods. In summary, the synergistic mechanism resulting from the integration of low-rank decomposition, *TV* regularisation and the Huber robust loss yields significant results. The method proposed in this paper achieves a superior trade-off between high fault detection and low false alarm rates, and demonstrates superior performance in fault classification at each sampling point compared to the listed comparison algorithms.

To further and more systematically verify the advantages of the method described in this paper in terms of detection accuracy, quantitative analyses were conducted on the fault detection results of the six methods at each sampling point, based on metrics such as *TP*, *FP*, *TN*, *FN*, *Precision*, *Recall*, *F1* and *FPR*. The results are as follows:

Table 2 Comparison of Accuracy Metrics for Fault Detection at Individual Sampling Points

Method	TP	FP	TN	FN	Precision	Recall	F1	FPR
Independent Estimation	568	889	4943	0	0.390	1.000	0.561	0.1524
Least Squares Thresholding	568	1362	4470	0	0.294	1.000	0.455	0.2335
Kalman Filter	542	448	5384	26	0.547	0.954	0.696	0.0768
Gaussian Bayesian	545	431	5401	23	0.558	0.960	0.706	0.0739
Standard RPCA	551	297	5535	17	0.650	0.970	0.778	0.0509
Proposed Method	558	85	5747	10	0.868	0.982	0.921	0.0146

Table 2 quantifies the overall fault detection performance of the various algorithms. Traditional fitting-based methods lack an anomaly suppression mechanism and are highly prone to misclassifying minor system drifts as faults, resulting in poor false alarm rates; Kalman and Gaussian Bayesian methods are constrained by the Gaussian noise assumption and exhibit detection lag when faced with sudden faults; standard *RPCA* relies solely on low-rank decomposition and lacks temporal smoothing constraints, making it prone to false alarms caused by short-term disturbances. This paper combines low-rank, sparsity and time-domain *TV* regularisation with the Huber robust loss, achieving an *F1* score of 0.922 and a false alarm rate of only 1.46 per cent. Whilst ensuring a high fault recall rate of 98.2 per cent, it significantly suppresses false alarms, with overall fault detection performance superior to all comparison schemes. The synergistic effect of these three types of constraints enables the complete capture of fault features whilst filtering out meaningless transient fluctuations.

3.3 Fault Detection Performance Indicator 2: Comparison of Detection Latency

For safety-critical systems such as the suspension system of maglev trains, fault detection must not only achieve a high detection accuracy but also produce a valid determination promptly after a fault occurs. Therefore, this paper employs the Average Detection Delay (ADD) [33] to evaluate the fault response speed of different methods. Detection delay is defined as the time difference between the actual time of fault occurrence and the time when the algorithm first outputs a valid fault determination. For the th controlled fault instance, its detection delay can be expressed as:

$$d_j = t_j^{\mathrm{det}} - t_j^{fault} \tag{37}$$

In the equation, t_j^{fault} denotes the actual time of occurrence of the j-th fault instance, and $t_j^{\det}$ denotes the time at which the algorithm first satisfies the predefined fault detection criteria. Taking the arithmetic mean of the detection delays for all N_f controlled fault instances yields:

$$ADD = \frac{1}{N_f}\sum_{j=1}^{N_f} d_j \tag{38}$$

To ensure consistency in comparisons between different methods, this paper calculates detection latency using the same controlled fault instances, fault onset times and valid judgement criteria. It should be noted that *ADD* reflects the statistical response time from the occurrence of a fault to the algorithm reaching a valid judgement; it does not include programme execution time on a specific in-vehicle computing platform and therefore cannot be directly equated with the end-to-end computational latency of an actual in-vehicle diagnostic system.

This paper employs a comparison of detection delays to evaluate the relative response speeds of six methods for three controlled fault channels. The starting point of the detection delay is defined as the moment the fault occurs, i.e. the sample point at which the gain first deviates from the normal range [0.9, 1.1]; the end point is defined as the moment when the method first outputs a valid fault detection signal. To illustrate the differences between the various methods in terms of the timeliness of fault confirmation, this paper selects the detection process of controlled fault channels as the subject of analysis and conducts a comparative analysis of the fault identification timelines for the six methods:

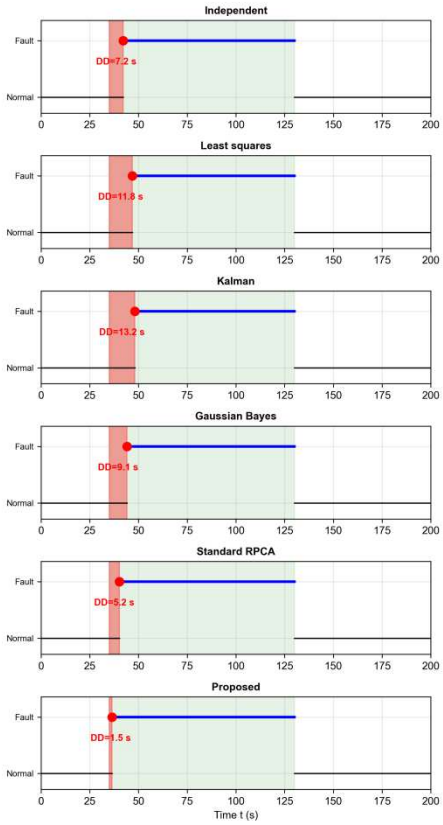

Figure. 2 Comparison of fault detection times for Channel 1 under six methods: (a) Independent method; (b) Least squares method; (c) Kalman + Cumulative Sum (CUSUM); (d) Gaussian Bayesian; (e) Standard RPCA; (f) The method proposed in this paper (low-rank + TV)

Figure 2 shows the fault detection timelines for Channel 1 under the six methods. The green shading indicates the controlled fault interval, the red shading indicates the detection delay between the onset of the fault and the first valid determination, and the blue solid line indicates the fault status output following the formation of a

valid determination. As can be seen from the figure, there are differences in the response times of the various methods following the onset of the fault. The independent estimation and least squares methods are relatively sensitive to observational fluctuations and are more easily affected by background variations; the Kalman filter and Gaussian Bayesian methods improve decision stability through recursive estimation or probabilistic modelling, but their response speed remains subject to the estimation process and noise assumptions; standard robust principal component analysis (RPCA) is able to utilise low-rank – sparse structures to separate background variations from local anomalies, but as it does not explicitly utilise time-domain total variance constraints, short-term fluctuations may still occur near the fault boundary.

By contrast, the method proposed in this paper combines low-rank structures, sparse fault components, the Huber robust loss function and time-domain total variation constraints, with the aim of suppressing global common-mode variations and transient disturbances whilst preserving the abrupt characteristics of local faults. Based on the existing simulation results, the detection delay for Channel 1 is 1.5 s, indicating that this method is capable of producing valid decisions relatively quickly under the current controlled fault scenario. This result reflects the detection performance for a specific channel and operating condition; a comprehensive evaluation must still be conducted in conjunction with results from other fault channels.

To further quantify these differences in delay, the six methods were tested on three controlled fault channels, yielding results for delay and average detection delay (ADD). The results are shown in the table below:

Table 3 Six methods for detecting delays across three controlled fault channels, and a summary of the average detected delays

Method	Ch.1（35–130 s）	Ch.3（58–145 s）	Ch.10（20–108 s）	ADD	Maximum Delay
Independent Estimation	7.2	5.8	8.1	7.03	8.1
Least Squares Thresholding	11.8	10.2	9.5	10.50	11.8
Kalman Filter	13.2	11.5	10.8	11.83	13.2
Gaussian Bayesian	9.1	7.8	7.5	8.13	9.1
Standard RPCA	5.2	5.8	4.8	5.27	5.8
Proposed Joint Methodology of this paper	1.5	1.7	1.2	1.47	1.7

Table 3 summarises the detection delays of the six methods across the three controlled fault channels: Ch.1, Ch.3 and Ch.10. Based on the data presented in the table, the detection delays for the three channels using the method proposed in this paper are 1.5 s, 1.7 s and 1.2 s, respectively, with an average of 1.47 s.

The delays for the three channels of the standard RPCA are 5.2 s, 5.8 s and 4.8 s, with an average of approximately 5.27 s; the delays for the three channels of the Kalman filter are 13.2 s, 11.5 s and 10.8 s, with an average of approximately 11.83 s. To ensure consistency in statistical analysis, this paper recalculates the average values for each method based on the delays of the three channels shown in the table, and evaluates the timeliness of detection accordingly.

The reduction in detection latency achieved by the method described in this paper, relative to the comparison method, is defined as

$$\eta = \frac{ADD_{bose} - ADD_{proposed}}{ADD_{base}} \times 100\% \tag{39}$$

Based on the channel-level data calculations described above, under the fault magnitude, noise level and decision rules used in the simulations in this paper, the method proposed herein reduces the average detection delay by approximately 72.2 per cent compared with standard RPCA, and by approximately 87.6 per cent

compared with Kalman filtering. The results indicate that, under the current simulation settings and a unified statistical framework, the method proposed in this paper exhibits a shorter fault detection delay. This is potentially attributable to the fact that low-rank components characterise common-mode variations across multiple channels, whilst sparse components highlight local anomalies; furthermore, the time-domain total variance constraint helps to reduce transient fluctuations near the fault boundary, thereby enabling fault detection to focus on persistent local anomalies.

It should be noted that the aforementioned delay results are based on the dynamic model, controlled fault range and decision rules established in this paper. Should there be changes in fault amplitude, noise intensity, controller compensation behaviour or model parameters, the algorithm's detection delay may vary accordingly. Therefore, this paper interprets these results as a relative performance comparison under the current simulation conditions, rather than directly extrapolating them to the timeliness of online diagnostics for vehicles in actual operation.

3.4 Fault Detection Performance Metric 3: Comparison of Robustness in Parameter Estimation

Fault detection performance depends not only on the classification model itself, but is also closely related to the accuracy of the prior gain parameter estimation. When sensor anomalies, burst noise or other outliers are present in the observed data, the parameter estimation results may be biased, which in turn affects subsequent fault classification. To evaluate the robustness of parameter estimation under abnormal observation conditions for different methods, this paper compares the changes in gain estimation bias across these methods by varying the proportion of outliers in the simulated data.

Suppose the true gain value of the k-th sample is g_k^{true}, and the corresponding estimated value is $\hat{g}_k$; in this case, the mean absolute bias is adopted as the evaluation metric, defined as

$$Bias = \frac{1}{N}\sum_{k=1}^{N}|\hat{g}_k - g_k^{true}| \tag{40}$$

In the formula, *N* represents the number of valid gain estimation samples included in the statistics; this refers to the channel-time points where the theoretical force is non-zero and the gain ratio can be reliably calculated. This is distinct from the total number of observation time sampling points and the number of independent replicate experiments. The smaller the value, the smaller the mean absolute deviation between the estimate and the true gain. To ensure fairness in the comparison between methods, all methods should employ the same test data, outlier injection method, outlier proportion and statistical interval.

Firstly, to provide a visual comparison of the performance of different algorithms in parameter estimation under conditions where outliers are present, this paper selects a simulation scenario with an outlier proportion of 7.5 per cent and conducts a visual analysis of the estimation results for the six methods, as shown in Figure 3.

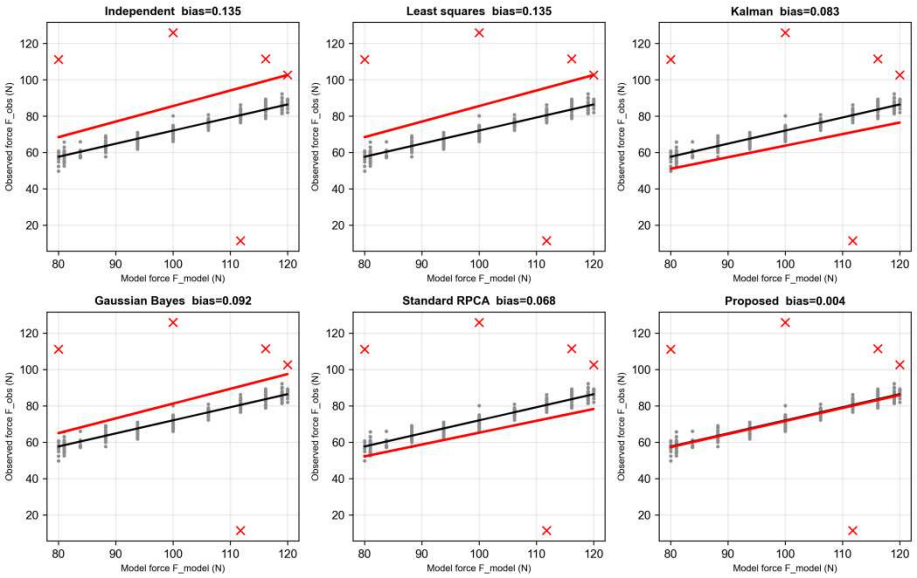

Figure. 3 Fitting results under a 7.5 per cent outlier threshold: (a) Independent method; (b) Least squares method ; (c) Kalman method(d) Gaussian Bayesian (e) Standard RPCA (f) Method proposed in this paper: Student's t-test

As can be seen from Figure 3, when the proportion of outliers is 7.5 per cent, there are marked differences in the parameter estimation results obtained by the various methods. The *Bias* for both independent estimation and the least squares method is 0.135, indicating that, under the current simulation conditions, the estimation results of both methods are significantly affected by anomalous observations. The biases of the Kalman filter and the Gaussian Bayesian method were 0.083 and 0.092 respectively, indicating that the introduction of a statistical estimation mechanism can reduce estimation bias to a certain extent, though the influence of outliers has not been completely eliminated. The *Bias* of the standard RPCA was further reduced to 0.068, suggesting that utilising low-rank–sparse structure to separate outlier information can improve parameter estimation performance; however, the estimation results still exhibit some bias.

By comparison, the Student's t-robust estimation method adopted in this paper exhibits a *Bias* of merely 0.004 in this scenario, which is significantly lower than that of the other methods under consideration. A comparison of the estimated curves with the reference true values in each sub-graph reveals that the estimation results obtained by this method deviate only slightly from the true benchmark, indicating that the Student's t-likelihood effectively mitigates the influence of outlier samples on parameter estimation under the current conditions of anomalous observations. However, results based on a single outlier proportion can only reflect the algorithm's performance at a specific level of anomaly intensity and are insufficient to fully demonstrate its stability across different levels of anomaly; therefore, further analysis is required to examine how *Bias* varies with the outlier proportion.

To investigate the impact of variations in the intensity of outliers on parameter estimation, this paper further sets the proportion of outliers at 0 per cent, 2.5 per cent, 5 per cent, 7.5 per cent, 10 per cent and 15 per cent, calculates the *Bias* of each method under different outlier conditions, and plots the resulting curves, as shown in Figure 4.

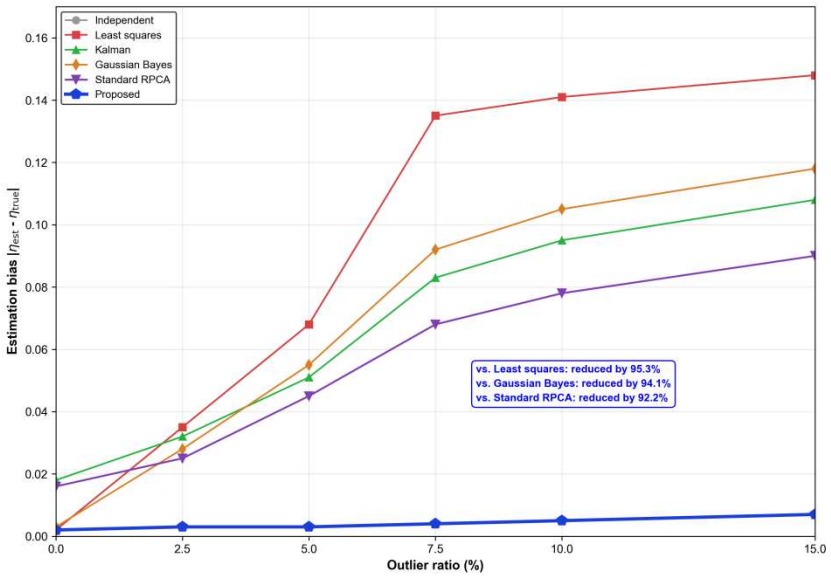

Figure. 4 Curves showing changes in bias at different outlier proportions

Figure 4 illustrates the trends in parameter estimation bias across the various methods as the proportion of outliers increases from 0% to 15%. Overall, the *Bias* for independent estimation, the least squares method, the Kalman filter, Gaussian Bayesian estimation and standard RPCA all increase to varying degrees as the proportion of outliers rises, reflecting the fact that anomalous observations cause varying degrees of interference with parameter estimation across different algorithms. In particular, the increase in bias was more pronounced for independent estimation and the least squares method, indicating that relying solely on conventional estimation mechanisms is insufficient to fully mitigate the impact of a steadily increasing proportion of outliers. Whilst the bias for the Kalman filter, Gaussian Bayesian and standard RPCA was generally lower than that of independent estimation and the least squares method, significant estimation errors still occurred when the proportion of outliers was high.

Compared with the methods described above, the method proposed in this paper consistently maintains a low bias within the tested outlier range of 0% – 15%; the value increases from 0.002 in the absence of outliers to 0.007 when the outlier proportion reaches 15%, representing a relatively small change. In particular, when the outlier proportion is 7.5 per cent, the bias is only 0.004, which is consistent with the estimation results shown in Figure 3. This phenomenon indicates that, under the current simulation settings, the Student’s t-robust estimation method is able, to a certain extent, to reduce the sensitivity of the estimation results to changes in the proportion of outliers. At the same time, in the scenario with no outliers, the bias of the method proposed in this paper is 0.002, which is identical to that of independent estimation and the least squares method, indicating that it does not exhibit any significant loss of accuracy under normal operating conditions in the current test.

To further quantitatively verify the differences illustrated in Figures 3 and 4, this paper calculated the bias of the six methods under different outlier proportions; the results are shown in Table 4.

Table. 4 Summary of quantitative results on the bias in gain estimates for each method under different proportions of outlier data

Outlier Proportion	Independent Estimation	Least Squares	Kalman Filter	Gaussian Bayesian	Standard RPCA	Proposed Method
0%	0.002	0.002	0.018	0.003	0.016	0.002
2.50%	0.035	0.035	0.032	0.028	0.025	0.003
5.00%	0.068	0.068	0.051	0.055	0.045	0.003
7.50%	0.135	0.135	0.083	0.092	0.068	0.004

10.00%	0.141	0.141	0.095	0.105	0.078	0.005
15.00%	0.148	0.148	0.108	0.118	0.090	0.007

As can be seen from Table 4, when the outlier proportion is 2.5 per cent, the *Bias* for both the independent estimation and the least squares method is 0.035; when the outlier proportion increases to 7.5 per cent, the *Bias* for both methods reaches 0.135; and under conditions of 15 per cent outliers, it rises further to 0.148. By comparison, the *Bias* of standard RPCA under the same outlier proportions was 0.025, 0.068 and 0.090, respectively. This indicates that low-rank–sparse decomposition can, to a certain extent, mitigate the *Bias* in parameter estimates caused by anomalous observations; however, as the proportion of anomalous samples increases further, estimation errors will still accumulate.

In a highly anomalous scenario where the proportion of outliers is 15 per cent, the *Bias* of the method proposed in this paper is 0.007, which is lower than that of the least squares method (0.148), the Gaussian Bayesian method (0.118) and standard RPCA (0.090). Based on the *Bias* under the same test conditions, the reduction in bias achieved by the method proposed in this paper compared with the least squares method, the Gaussian Bayesian method and standard RPCA is 95.3 per cent, 94.1 per cent and 92.2 per cent, respectively.

The above results indicate that, under the current set of strong outlier conditions, the method proposed in this paper is capable of significantly reducing bias in gain estimation. Taking into account the comparison of single operating conditions in Figure 3, the trend in the proportion of outliers across different scenarios in Figure 4, and the quantitative results in Table 4, it can be seen that the method proposed in this paper exhibits good stability in parameter estimation under the tested outlier scenarios. Its advantages are primarily reflected in low estimation *Bias* and a relatively limited increase in bias as the proportion of outliers rises.

It should be noted that *Bias* measures the deviation between the parameter estimate and the true gain, whilst the *F1* score and false positive rate measure the consistency between fault classification results and true labels; these three metrics correspond to different evaluation objectives. Therefore, this paper uses *Bias*, the *F1* score and the false positive rate separately to evaluate parameter estimation and fault recognition performance, thereby avoiding the use of a single metric as a substitute for a comprehensive evaluation of the entire diagnostic process. Furthermore, the current conclusions regarding robustness are only applicable to the outlier proportions, anomaly amplitudes and simulation models tested in this paper; they cannot yet be directly extrapolated to arbitrary noise distributions or conditions of model structural mismatch.

3.5 Comparison of Ablation Experiments with Electromagnetic Force Models

The methodology presented in this paper comprises four key design elements: the Student’s t-distribution noise assumption, the Huber loss, low-rank sparse decomposition, and TV temporal regularisation. Among these, the Student’s t-likelihood is applied during the parameter inversion stage; its contribution to counteracting outliers has already been demonstrated in the bias comparison experiments presented in Table 4 above. The Huber loss, acting as the data fidelity term for the low-rank sparse decomposition, works in conjunction with the decomposition itself to form a robust decomposition. To quantitatively evaluate the contributions of the two structured constraints—low-rank sparsity and total variance in the time domain—within the joint decomposition model, this section presents three sets of ablation experiments.

Control group 1: Basic Bayesian + Least Squares (no low-rank sparsity, no TV)

Control group 2: Basic + Low-rank Sparse Decomposition (with TV temporal constraints removed)

Control group 3: The complete model proposed in this paper (with TV temporal constraints included)

Using *F1* score, false positive rate (*FPR*), average detection delay (*ADD*) and bias under the 15 per cent outlier threshold as ablation evaluation metrics, the ablation results are shown in Table 5.

Table. 5 Comparison of quantitative indicators from ablation experiments (under 15 per cent outlier conditions)

Ablation Group	Configuration Description	F1	FPR/%	ADD/s	Bias under 15%

					Outliers
1	Only Bayesian Least Squares	0.455	23.35	10.5	0.148
2	+Low-Rank Sparse Decomposition	0.852	3.21	3.1	0.026
3	Full Model (+ Temporal TV Regularization)	0.922	1.46	1.47	0.007

As shown in Table 5, after incorporating low-rank sparse decomposition, the F1 score improved from 0.455 to 0.852, the FPR decreased from 23.35 per cent to 3.21 per cent, the ADD was reduced from 10.5 s to 3.1 s, and the bias fell from 0.148 to 0.026; further incorporating TV temporal constraints resulted in an F1 score of 0.922, an FPR of 1.46 per cent, an ADD of 1.47 seconds and a bias of 0.007. This demonstrates that low-rank sparse decomposition achieves signal decoupling by separating global common-mode drift from local faults, whilst TV regularisation further enhances detection accuracy and timeliness by preserving fault transition boundaries and suppressing short-term fluctuations; it is only through the synergistic effect of these two structured constraints that high-precision, low-latency and highly robust multi-channel fault identification can be achieved.

Furthermore, in the first stage of modelling, this paper compares the proposed model with a traditional unconstrained SINDy baseline model under identical training conditions, in order to quantify the improvement in the electromagnetic force model achieved through the application of physical constraints. Table 6 summarises the fitting accuracy and physical consistency of the two models. The root mean square error (RMSE) of the unconstrained SINDy model is slightly lower, at 0.0536 (coefficient of determination R^2 = 0.9983); however, this model violates the electromagnetic monotonicity law within a 5.21 per cent operating range. Almost all violations correspond to spurious positive derivatives in the large-gap region, where higher-order polynomial terms cause the force characteristic curve—which should be decreasing—to rise. In contrast, the physically constrained model reduces the monotonicity violation rate to 0.00 per cent, whilst the fitting accuracy decreases accordingly: the RMSE rises from 0.0536 to 0.0600 (a relative increase of approximately 11.9 per cent), and R^2 falls from 0.9983 to 0.9979 (a decrease of 0.0004). This result quantitatively demonstrates that embedding partial derivative inequality constraints in sparse symbolic regression enables the enforcement of objective electromagnetic laws whilst preserving modelling accuracy, thereby eliminating non-physical interpretations that would otherwise propagate to downstream Bayesian inversion and fault location stages.

Table 6 Fitting Accuracy and Physical Consistency of Electromagnetic Force Models

Model	RMSE	R^2	MVR (%)
Unconstrained SINDy (STLSQ)	0.0536	0.9983	5.21
Physics-constrained (proposed)	0.0600	0.9979	0.00

3.6 Engineering Applicability, Robustness and Limitations of Simulation Validation

This paper constructs a dynamic simulation model of the suspension system based on publicly available technical parameters and relevant literature. The proposed method is numerically validated under controlled operating conditions, including observation noise, outliers, global gain drift and local gain anomalies. Through standardised data partitioning, fault configuration and evaluation metrics, the performance of various methods is compared in terms of fault identification accuracy, detection delay and parameter estimation bias. Numerical simulation provides a testing environment with clearly defined fault ground truth and controllable disturbance intensity; however, the applicability of the conclusions remains limited by the model structure, parameter settings and the extent of operational condition coverage.

Under the tested conditions, the method proposed in this paper achieved an *F1* score of 0.922, a false alarm

rate of 1.46 per cent, and a gain estimation bias of 0.007 under a 15 per cent outlier threshold. The above results are based on the assumption that the data-generating model and the inverted model share the same dynamic structure. However, factors such as deviations in dynamic parameters, unmodelled electromagnetic coupling and sensor dynamics may lead to model mismatch, thereby affecting the accuracy of gain inversion. To investigate this effect, parameter perturbation experiments were conducted in this paper.

Furthermore, the above results are based on open-loop dynamic simulations and do not explicitly incorporate a closed-loop suspension controller. In actual systems, the controller may compensate for the gain reduction in the power amplifier by adjusting the current, thereby attenuating the fault features in the observed signal. To investigate this effect, a closed-loop simulation model was established in this paper.

(1)Model mismatch verification. A two-degree-of-freedom dynamic model was employed in both the data generation and inversion stages; however, the key physical parameters in the generation stage (vehicle body mass, suspension mass, air spring stiffness and secondary system damping) were perturbed by 5 per cent, 10 per cent, 15 per cent and 20 per cent, respectively, relative to those in the inversion stage, to investigate the impact of parameter mismatch in the inversion model on gain estimation. The true gain value was set at 0.72 (simulating a gain attenuation fault of approximately 28 per cent), with observation noise set at 2.5 per cent of the standard deviation. The bias in gain estimation under different parameter perturbation levels is shown in Table 7.

Table 7 Bias in gain estimation under model mismatch

Parameter perturbation level (%)	Gain estimation bias	Relative error (%)
0	0.0002	0.03
5	0.0345	4.8
10	0.0653	9.1
15	0.0937	13.0
20	0.1201	16.7

As can be seen from Table 7, the bias in the gain estimate is only 0.0002 when there is no parameter mismatch; when the parameter perturbation reaches 5 per cent, 10 per cent, 15 per cent and 20 per cent, the bias increases to 0.0345, 0.0653, 0.0937 and 0.1201 respectively, with the relative error rising monotonically from 4.8 per cent to 16.7 per cent. This indicates that gain inversion is relatively sensitive to deviations in the parameters of the dynamic model; parameter mismatch introduces systematic estimation bias, and this bias increases approximately linearly with the degree of mismatch.

(2)Closed-loop control verification. This paper employs a representative PID suspension controller (proportional gain K_p = 3000, integral gain K_i = 300, derivative gain K_d = 100, current limit [0, 60] A, sampling period 2 ms), which adjusts the suspension current via feedback to maintain the set suspension clearance. It should be noted that this controller is a representative simulation controller used in this paper and is not a verified actual train controller. Under closed-loop conditions, power amplifier gain attenuation ranging from 5% to 40% was introduced to investigate the impact of controller compensation on fault detectability; the results are shown in Table 8.

Table 8 Test results for different gain attenuation levels under closed-loop operating conditions

Gain attenuation (%)	Open-loop gap offset (m)	Closed-loop gap offset (m)	Closed-loop current (A)	Inverse Gain Estimation
0	0.0000	0.0000	20.00	1.0000
15	0.0070	0.0039	20.75	0.8504
25	0.0121	0.0042	22.03	0.7505
40	0.0203	0.0043	24.60	0.6001

As can be seen from Table 8, under open-loop conditions, gain attenuation leads directly to a significant deviation in the suspension gap (approximately 0.020 m when attenuation is 40 per cent); under closed-loop

conditions, the PID controller compensates by increasing the suspension current (from 20.00 A to 24.60 A), thereby limiting the shift in the suspension gap to approximately 0.004 m; that is, the controller’s compensation significantly attenuates the fault characteristics observed in the gap measurement. However, as the method described in this paper estimates gain via dynamic inversion—a process that simultaneously utilises the compensated current information—the estimated gain still accurately reflects the true gain (the estimated gain at 40 per cent attenuation is 0.6001, consistent with the true value of 0.60). Using a 3 per cent gain reduction as the detection threshold and observation noise equivalent to 2.5 per cent of the standard deviation, and under operational criteria of $Recall \geqslant 0.95$ and $FPR \leqslant 5$ per cent, the minimum detectable gain reduction under closed-loop conditions is approximately 5–6 per cent.

The above results indicate that a mismatch in model parameters leads to a gain estimation bias that increases approximately linearly with the degree of mismatch; consequently, results obtained under nominal model conditions cannot be directly extrapolated to conditions of parameter mismatch. In contrast, the gain estimation obtained using the method described in this paper is not significantly affected by controller compensation and can still reliably detect power amplifier gain degradation under closed-loop conditions. It should be noted that the two-degree-of-freedom vertical dynamic model adopted in this paper is intended to establish a low-order inverse relationship between the measurable signal and the observed electromagnetic force; it is not intended to fully reproduce all the high-order dynamic behaviour of an actual maglev train. Unmodelled factors, such as multi-channel electromagnetic coupling, vehicle pitch and roll, and sensor dynamic errors, may still influence the observed signal; Furthermore, whilst the closed-loop validation utilised a representative PID controller, the minimum detectable gain attenuation value depends on the controller employed, the noise level and the detection criteria; the threshold for actual train closed-loop systems still requires further confirmation via a hardware-in-the-loop platform and de-sensitised experimental data.

4.Conclusion

Addressing issues such as the non-linear modelling of electromagnetic forces, the susceptibility of parameter estimation to interference under heavy-tailed noise, and the underdetermined nature of multi-channel time-varying gain inversion in the identification of gain anomalies in the power amplifiers of maglev train suspension systems, this paper constructs a progressive fault identification framework comprising electromagnetic force modelling based on physical constraints, robust Bayesian inversion, and a joint decomposition of low-rank, sparse and time-domain total error. The performance of this method under specified operating conditions was analysed through open-loop parameter-driven numerical simulations and comparative experiments. The main conclusions are as follows.

(1) With regard to the modelling of electromagnetic forces, this paper introduces electromagnetic monotonicity constraints into the sparse symbolic regression model to balance model fitting accuracy with physical consistency. The current results show that the unconstrained SINDy model has a coefficient of determination of 0.9983, a root mean square error of 0.0536, and a monotonicity violation rate of 5.21 per cent; the physically constrained model has a coefficient of determination of 0.9979, a root-mean-square error of 0.0600, and a monotonicity violation rate reduced to 0.00 per cent. This indicates that, within the scope of the current data and the constraint domain, physical constraints can effectively minimise non-physical fitting behaviour, thereby providing a physically consistent electromagnetic force model for subsequent parameter inversion.

(2) In terms of fault detection, the joint decomposition method proposed in this paper achieved an F1 score of 0.922 and a false alarm rate of 1.46 per cent on the current simulation data; when the proportion of outliers was

15 per cent, the bias in gain estimation was 0.007. From a methodological perspective, the Student’s t-likelihood, Huber robust loss, low-rank decomposition and time-domain total variance constraint are applied to the estimation of heavy-tailed noise, suppression of anomalous residuals, cross-channel structural separation and time continuity constraints, respectively. This paper conducts multiple sets of ablation experiments to quantitatively analyse the contributions of low-rank sparse decomposition and the time-domain total variance constraint; the results indicate that the stepwise introduction of these two structured constraints can consistently improve the overall performance of fault detection. It should be noted that, under the current underdetermined observation conditions, this method is limited to the identification of gain anomalies in power amplifiers and cannot achieve automatic, complete isolation of multiple fault types, such as power amplifier faults, sensor offset, or changes in vehicle body mass. The aforementioned results merely support the validity of the method described in this paper within the tested noise and fault scenarios; they do not imply that it possesses the same performance advantages for arbitrary model errors or in real-world operational environments.

(3) With regard to the timeliness of fault detection, this paper calculates the detection delay based on the time difference between the moment the fault occurs and the moment of the first valid detection. According to the delay data for the three controlled fault channels listed in Table 3, the average detection delay of the method proposed in this paper should be uniformly calculated as 1.47 s; the average detection delays for standard RPCA and Kalman filtering are approximately 5.27 s and 11.83 s, respectively. Calculated using this statistical approach, the average detection delay of the method proposed in this paper is reduced by approximately 72.2 per cent compared with standard RPCA, and by approximately 87.6 per cent compared with the Kalman filter. This result demonstrates that, solely under controlled simulation scenarios with the current fault amplitude and noise levels, the proposed method is capable of producing fault determinations relatively quickly.

It should be noted that the validation level of this paper is based on numerical simulation using publicly available parameters, and the research conclusions are primarily applicable to the established dynamic model and the range of disturbances tested. Factors such as model structural mismatch, controller compensation, multi-channel electromagnetic coupling and sensor dynamic characteristics may still alter the distinguishability and detection timeliness of gain anomalies. Therefore, whilst this paper has verified the impact of model mismatch and controller compensation on algorithm performance through parameter perturbation and closed-loop simulation, the detectable thresholds for actual train closed-loop systems still require further confirmation via hardware-in-the-loop platforms and de-sensitised experimental data.

References

1. Lee HW, Kim KC, Lee J. Review of maglev train technologies. IEEE Transactions on Magnetics. 2006;42(7):1917-1925.

2. Deng ZG, Liu ZX, Li HT, et al. Development status and prospect of maglev trains. Journal of Southwest Jiaotong University. 2022;57(3):455-474. https://doi.org/10.3969/j.issn.0258-2724.20220001

3. Zhao Y, Ji CW, Yang Y, et al. Dynamical behavior of HTS maglev system over a NdFeB guideway with a fluctuant field distribution. IEEE Transactions on Applied Superconductivity. 2019;29(3):3601905. https://doi.org/10.1109/TASC.2018.2882222

4. Zhai W, Wang K, Cai C. Fundamentals of vehicle-track coupled dynamics. Vehicle System Dynamics. 2009;47(11):1349-1376.

5. Sinha PK. Electromagnetic Suspension: Dynamics and Control. London: IET; 1987.

6. Wang LC, Yu PC, Li JH, et al. Suspension system status detection of maglev train based on machine learning using levitation sensors. In: Proceedings of the 29th Chinese Control and Decision Conference. 2017:5184-5189. https://doi.org/10.1109/CCDC.2017.7978559

7. Ding J, Yang X, Long Z, et al. Three-dimensional numerical analysis and optimization of electromagnetic suspension system for 200 km/h maglev train considering eddy current effect. IEEE Access. 2018;6:61547-61555. https://doi.org/10.1109/ACCESS.2018.2876599

8. Mukhopadhyay SC, Ohji T, Iwahara M, et al. Modeling and control of a new horizontal-shaft hybrid-type magnetic bearing. IEEE Transactions on Industrial Electronics. 2000;47(1):100-108. https://doi.org/10.1109/41.824131

9. Sun Y, Xu J, Lin G, et al. Adaptive neural network control for maglev vehicle systems with time-varying mass and external disturbance. Neural Computing and Applications. 2021;33(17):12361-12372. https://doi.org/10.1007/s00521-021-05874-2

10. Raissi M, Perdikaris P, Karniadakis GE. Physics-informed neural networks: a deep learning framework for solving forward and inverse problems involving nonlinear partial differential equations. Journal of Computational Physics. 2019;378:686-707.

11. Brunton SL, Proctor JL, Kutz JN. Discovering governing equations from data by sparse identification of nonlinear dynamical systems. Proceedings of the National Academy of Sciences. 2016;113(15):3932-3937.

12. Li HT, Deng ZG, Huang H, et al. Experiments and simulations of the secondary suspension system to improve the dynamic characteristics of HTS maglev. IEEE Transactions on Applied Superconductivity. 2021;31(6):3602508. https://doi.org/10.1109/TASC.2021.3091070

13. Goldstein H, Poole CP, Safko JL. Classical Mechanics. 3rd ed. Boston: Addison-Wesley; 2002.

14. Nelles O. Nonlinear System Identification: From Classical Approaches to Neural Networks. Berlin: Springer; 2001.

15. Kalman RE. A new approach to linear filtering and prediction problems. Journal of Basic Engineering. 1960;82(1):35-45.

16. Gelman A, Carlin JB, Stern HS, et al. Bayesian Data Analysis. 3rd ed. Boca Raton: CRC Press; 2013.

17. Lange KL, Little RJA, Taylor JMG. Robust statistical modeling using the t distribution. Journal of the American Statistical Association. 1989;84(408):881-896.

18. Candès EJ, Li X, Ma Y, et al. Robust principal component analysis? Journal of the ACM. 2011;58(3):1-37.

19. Cui YP, She LH, Li XL, et al. Fault diagnosis for suspension signal of maglev vehicle based on mathematical model. Applied Mechanics and Materials. 2012;190-191:987-992. https://doi.org/10.4028/www.scientific.net/AMM.190-191.987

20. Li Y, He G, Li J. Nonlinear robust observer-based fault detection for networked suspension control system of maglev train. Mathematical Problems in Engineering. 2013;2013:713560. https://doi.org/10.1155/2013/713560

21. Wu L, Zhou R, Yang G, et al. Research on fault diagnosis of electromagnetic active suspension based on double observer intelligent switching. Proceedings of the Institution of Mechanical Engineers, Part D: Journal of Automobile Engineering. 2025;239(7):2964-2981. https://doi.org/10.1177/09544070241232743

22. Kandil A. Modeling and control of rotor oscillations in active magnetic bearings using a generalized pole-pair approach. Journal of Nonlinear Mathematical Physics. 2026;33(1):52. https://doi.org/10.1007/s44198-026-00397-7

23. Ibrahim MMM, Elsaid A, Zahra WK, et al. Vertical and lateral oscillations of a MAGLEV vehicle: aerodynamic effects and integral resonant control. Journal of Vibration Engineering & Technologies. 2026;14(5):222. https://doi.org/10.1007/s42417-026-02427-6

24. Ibrahim MMM, Kandil A, Zahra WK, et al. Elimination of the vibration center shift in the nonlinear oscillations of a MAGLEV vehicle subjected to steady and unsteady aerodynamic forces: second-order multiple scales analysis. ZAMM-Journal of Applied Mathematics and Mechanics. 2025;105:e70125.

https://doi.org/10.1002/zamm.70125

25. Kandil A. Nonlinear dynamic behavior, impact suppression, and stability control of rotor active magnetic bearing systems: a comparative study of fixed and adjustable surplus current strategies. European Journal of Mechanics-A/Solids. 2026;116:105928. https://doi.org/10.1016/j.euromechsol.2025.105928

26. Kandil A, Francis AC, Elsaid A, et al. Effect of the suspended block's weight on the nonlinear dynamics of a non-ideal magnetic levitation model connected to an energy harvester. International Journal of Non-Linear Mechanics. 2025;170:104974. https://doi.org/10.1016/j.ijnonlinmec.2024.104974

27. Francis AC, Zahra WK, Elsaid A, et al. Improvement of the non-periodic energy harvesting behavior of a non-ideal magnetic levitation system utilizing internal resonance. Journal of Vibration Engineering & Technologies. 2024;12(7):8363-8382. https://doi.org/10.1007/s42417-024-01364-6

28. Brooks S, Gelman A, Jones GL, et al. Handbook of Markov Chain Monte Carlo. Boca Raton: CRC Press; 2011.

29. Huber PJ. Robust Statistics. New York: Wiley; 1981.

30. Tibshirani R. Regression shrinkage and selection via the lasso. Journal of the Royal Statistical Society: Series B. 1996;58(1):267-288.

31. Salfner F, Lenk M, Malek M. A survey of online failure prediction methods. ACM Computing Surveys. 2010;42(3):1-42.

32. IEEE. IEEE standard for prognostics and health management (PHM) for electronic systems. IEEE Std 1856-2017; 2017.

33. Isermann R. Fault-Diagnosis Systems: An Introduction from Fault Detection to Fault Tolerance. Berlin: Springer; 2006.